

## THE EFFECT OF THE COSMIC WEB ON CLUSTER WEAK LENSING MASS ESTIMATES

CHRISTOPHER A. METZLER<sup>1,3</sup>, MARTIN WHITE<sup>1,4</sup> AND CHRIS LOKEN<sup>2,5</sup>

<sup>1</sup>Harvard Smithsonian Center for Astrophysics, 60 Garden St, MS-51, Cambridge, MA 02138

<sup>2</sup>Department of Physics and Astronomy, St. Mary's University, Halifax, Nova Scotia, CANADA

<sup>3</sup>cmetzler@cfa.harvard.edu

<sup>4</sup>mwhite@cfa.harvard.edu

<sup>5</sup>cloken@ap.stmarys.ca

*Draft version October 28, 2018*

### ABSTRACT

In modern hierarchical theories of structure formation, rich clusters of galaxies form at the vertices of a weblike distribution of matter, with filaments emanating from them to large distances and with smaller objects forming and draining in along these filaments. The amount of mass contained in structure near the cluster can be comparable to the collapsed mass of the cluster itself. As the lensing kernel is quite broad along the line of sight around cluster lenses with typical redshifts  $z_l = 0.5$ , structures many megaparsecs away from the cluster are essentially at the same location as the cluster itself, when considering their effect on the cluster's weak lensing signal. We use large-scale numerical simulations of structure formation in a  $\Lambda$ -dominated cold dark matter model to quantify the effect that large-scale structure near clusters has upon the cluster masses deduced from weak lensing analysis. A correction for the scatter in possible observed lensing masses should be included when interpreting mass functions from weak lensing surveys.

*Subject headings:* cosmology: theory — galaxies: clusters: general — gravitational lensing

### 1. INTRODUCTION

The masses of clusters of galaxies are now measurable by a variety of observational techniques. Most approaches require some equilibrium assumption which relates the shape of the cluster potential to the energy content of some cluster component. For example, measuring or mapping the temperature of the hot, X-ray emitting intracluster plasma, or the velocities of cluster galaxies, permits a prediction for the mass distribution of the cluster.

Another method for estimating cluster masses has been through observations of weak gravitational lensing of the background galaxy field by the cluster. The map of induced distortions in background galaxy ellipticities can in principle be inverted to provide a weighted sum of the mass density along the line of sight. The weighting is weakest near the lensed sources and near us, while it is strongest at intermediate redshifts where the cluster lens is typically located. Thus, this yields an estimate of the surface mass density distribution of the cluster and its surroundings, from which the cluster mass can be inferred. Since assumptions about the dynamical or thermodynamic state of the cluster components are of uncertain validity, while weak lensing analyses probe the mass distribution directly, estimating cluster masses through weak lensing analyses has grown extremely popular in the last decade. Several groups now have moderate samples of weak lensing masses (see e.g. Mellier 1999 for a recent review), while others have applied weak lensing mass estimates to studies of evolution in the cluster abundance (e.g. Bahcall & Fan 1998).

One interesting outcome of multi-wavelength studies of clusters has been that weak lensing mass estimates for clusters sometimes exceed mass estimates derived from other sources, typically X-ray observations (see e.g. Squires *et.al.* 1999). This discrepancy is often considered to be

*underestimated*, because methods for extracting the mass from weak lensing data typically depend on the estimated surface density relative to some value near the edge of the observing field, which may contain part of the cluster if the viewing field is small. When this discrepancy occurs, it is typically attributed to either the poor quality of the X-ray data involved — as good X-ray spectra and images become more difficult to obtain with increasing redshift — or to the failure of equilibrium assumptions about the state of cluster gas at high-redshift.

However, attempts to reconstruct the mass distribution of clusters from weak lensing observations are not without pitfalls (see e.g. Mellier 1999). The most well-known of these is associated with the typically uncertain redshift distribution of the lensed sources; still others relate to details of the procedure adopted to go from the observed ellipticity distribution to the mass, or from instrumental effects. We here consider another potential issue: the effect on mass estimates from clustered matter near the cluster and in the observing field.

In modern hierarchical models of structure formation, clusters form in overdense regions at the vertices of filamentary structures which extend to large distances from the cluster; they accrete additional mass and smaller collapsed objects that drain along these filaments. It is thus reasonable to expect a beaded filamentary structure surrounding most clusters of galaxies. Such overdense filamentary structure, when viewed in projection through its lensing effects, could add to the lensing signal produced by a cluster and result in an overestimate of the cluster mass; in fact, such an effect may have been identified in one cluster (Czoske *et.al.* 1999). In principle clusters could also be located near voids, leading to a deficit of material along the line of sight compared to the mean density. Tentative observational evidence of filamentary structure near clusters has been reported recently (Scharf *et.al.* 1999, Kull

& Boehringer 1999, Kaiser *et.al.* 1999). A filament lying near or intersecting with the line of sight will also lens the background galaxies, and therefore contribute spuriously to the lensing signal. If the observed lensing signal were attributed solely to the cluster, the inferred cluster mass could be much larger than its actual mass.

The impact of projection effects upon mass estimators has been studied in a variety of contexts (see *e.g.* van Haarlem *et.al.* 1997). The contamination of weak lensing mass estimates by nearby large-scale structure has been considered to varying degrees in other papers (see *e.g.* Miralda-Escude 1991; Cen 1997; Wambsganss, Cen & Ostriker 1998; Reblinsky & Bartelmann 1999). In a recent *Letter* (Metzler *et al.* 1999) we performed a preliminary study of this effect on three simulated clusters. We now broaden this work to consider more clusters and apply a more accurate modelling of the lensing signal produced by the simulated clusters. In §4, we examine how nearby large-scale structure affects mass estimates at mean interior density contrasts of 200 at a redshift of  $z_l = 0.5$ ; we also consider how this effect depends on cluster redshift and the density contrast within which masses are measured. In real situations, however, an observer is not concerned with the likelihood of finding a certain lensing mass given a value of the actual cluster mass; instead, what is desired is the likelihood distribution of a cluster’s *actual* mass, given an observation of the lensing mass. We consider this in §5. In §6, we consider the effect of this dispersion in possible observed lensing masses for a given actual mass upon the observed mass function of galaxy clusters. The possibility of avoiding this source of error by using line of sight velocity histograms to reject clusters with apparent foreground/background structure will be addressed in §7.1. Finally, we examine the contribution to this effect by material at successively larger distances from the cluster in §7.2.

## 2. LENSING THEORY

In the thin lens approximation, the convergence  $\kappa$  is related to the surface density  $\Sigma$  of the gravitational lens by

$$\kappa = \frac{\Sigma}{\Sigma_{\text{crit}}} = \frac{4\pi G}{c^2} \frac{D_{A,L} D_{A,LS}}{D_{A,S}} \Sigma \quad (1)$$

where  $D_{A,L}$ ,  $D_{A,S}$ , and  $D_{A,LS}$  refer to the angular-diameter distances to the lens and the lensed source, and the angular-diameter separation between lens and source, respectively. The convergence is related to the 2D lensing potential  $\psi$  by

$$\kappa = \frac{1}{2} \nabla_{\theta}^2 \psi, \quad (2)$$

with the lensing potential derived from the peculiar potential  $\phi$  induced by mass inhomogeneities by

$$\psi = \frac{2}{c^2} \int dD_L \frac{\phi}{a} \frac{D_{LS}}{D_L D_S} \quad (3)$$

where here the distances  $D_L$ ,  $D_S$ , and  $D_{LS}$  are *comoving*,  $a$  is the cosmic scale factor (scaled to 1 at present), and the integration is taken along the path travelled by the light ray. With some algebra, and the use of the first Friedmann equation and the Poisson equation for the peculiar

potential  $\phi$ , the convergence  $\kappa$  can therefore be written as

$$\kappa = \frac{3}{2} \Omega_m \left( \frac{H_0}{c} \right)^2 \int dD_L \frac{D_L D_{LS}}{D_S} \frac{\delta}{a}, \quad (4)$$

where  $\delta$  is the local overdensity in terms of the average density  $\bar{\rho}$ ,  $\delta = (\rho - \bar{\rho})/\bar{\rho}$ . For the specific case of flat universes,  $D_{LS} = D_S - D_L$ , and so we can write

$$\kappa = \frac{3}{2} \Omega_m \left( \frac{H_0 D_S}{c} \right)^2 \int dt t(1-t) \frac{\delta}{a}, \quad (5)$$

where  $t = D_L/D_S$ . Note that this derivation for the convergence along a particular line of sight assumes the lensed source(s) to be at a single redshift. For a distribution of sources one further integrates over  $\int dz_s n(z_s)$  where  $\int dn = 1$ .

This last equation, Eq. (5), is the main equation used in analyzing the simulation datasets. The important point is that the integrand can be thought of as the product of the overdensity and a lensing kernel. The width of the kernel, written here as  $t(1-t)$ , along the line of sight typically does not vary strongly for clusters at intermediate redshifts, even at large distances from the cluster lens. For instance, for a lens at  $z_l = 0.5$  and  $z_s = 1.0$ , over a distance of  $256 h^{-1} \text{Mpc}$  comoving centered on the cluster (the lengths of the lines of sight we will simulate), the lensing kernel varies from 96% to 102% of its central value in the flat  $\Lambda$ -dominated cosmology we are using. For a lens at  $z_l = 1.0$  and  $z_s = 1.5$ , the lensing kernel varies from 87% to 111% of its central value over the same distance. Therefore, mass concentrations out to large radii from the cluster can still contribute appreciably to the lensing signal.

## 3. METHOD

### 3.1. The Cluster Ensemble

To examine this effect, cosmological simulations including clusters as well as the large scale structure in which they are embedded are needed. Here we have used 12 clusters from the X-Ray Cluster Data Archive of the Laboratory for Computational Astrophysics of the National Center for Supercomputing Applications (NCSA), and the Missouri Astrophysics Research Group of the University of Missouri (Norman *et.al.* 2000). To produce these clusters, a particle-mesh N-body simulation incorporating adaptive mesh refinement was performed in a volume  $256 h^{-1} \text{Mpc}$  on a side. Regions where clusters formed were identified; for each cluster, the simulation was then re-run (including a baryonic fluid) with finer resolution grids centered upon the cluster of interest. In the adaptive mesh refinement technique, the mesh resolution dynamically improves as needed in high-density regions. The “final” mesh scale at the highest resolution was  $15.6 h^{-1} \text{kpc}$ , with a mean interparticle separation of about  $86 h^{-1} \text{kpc}$ , allowing good resolution of the filamentary structure around the cluster. The code itself is described in detail in Norman & Bryan (1999). Table 1 shows the mass within  $r_{200}$ , the radius containing material at a mean interior density contrast of 200, at redshifts of 0.5 and 1.0 for the 12 clusters in the ensemble.

The clusters used here were taken at redshifts of  $z = 0.5$  and  $z = 1.0$  from simulations of a  $\Lambda \text{CDM}$  model, with

TABLE 1  
CLUSTER MASSES WITHIN  $\bar{\delta} = 200$

Cluster	$M_{200}$ ( $10^{15} M_{\odot}$ )	
	$z = 0.5$	$z = 1.0$
0	0.83	0.24
1	0.86	0.64
2	0.35	0.23
3	0.58	0.25
4	0.70	0.25
5	0.52	0.27
6	0.52	0.38
7	0.48	0.38
8	0.61	0.40
9	0.64	0.26
10	0.38	0.12
11	0.55	0.25

parameters  $\Omega_m = 0.3$ ,  $\Omega_B = 0.026$ ,  $\Omega_{\Lambda} = 0.7$ ,  $h = 0.7$ , and  $\sigma_8 = 0.928$ . This dataset comprises the twelve most massive clusters at  $z = 0$ , as determined from the initial, low-resolution run. Their numbering is in order of  $z = 0$  virial mass; as each cluster evolves, this ranking in mass does not necessarily hold at higher redshifts.

All of the clusters in the ensemble were embedded in a larger filamentary network of structure. The filaments themselves were typically resolved by the simulation into a string of dense knots embedded in more diffuse material. In Fig. 1, we show a portion of a slice through the simulation volume, centered on cluster 6 at  $z = 0.5$ , at two successive levels of “zoom.” The filamentary structure in which the cluster is embedded is apparent, despite the limitations of the two-dimensional image. Since much of the mass in filaments is at comparatively low density contrast, the existence of this structure near the line of sight would not be easy to constrain by observations of redshifts near the cluster. We will examine this point further in §7.1

### 3.2. Analysis

For a specific line of sight through a simulated cluster, a map of the convergence  $\kappa$  was constructed by viewing the cluster and its surroundings through a  $40'$  square window. This window was then divided into a  $512 \times 512$  grid, and Eq. (5) was integrated up along the line of sight through each pixel to produce the final map.

A potential source of error lies in the integration path used. Formally, the integration should be performed along the perturbed path of a light ray, while we take the integration along the unperturbed path. However, outside the large density contrasts in the cores of clusters, we are in the weak lensing regime. The deflection  $\Delta y$  induced by crossing a perturbation over an effective scale  $\Delta z$  can be approximated by

$$\Delta y \simeq \frac{\phi}{c^2} \Delta z, \quad (6)$$

where  $\phi$  is the magnitude of the potential. The maximum value for  $\phi/c^2$  to be expected in the simulation volume is that of the typical value for rich clusters,  $10^{-5}$ . This suggests that the deflection in photon path induced by cross-

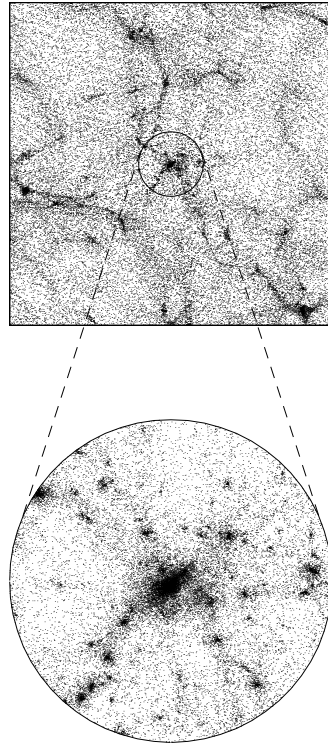


FIG. 1.— A slice through the simulation volume, showing simulated Cluster 6 at  $z = 0.5$ , at two levels of magnification. Dots represent simulation particles. The slice has a comoving thickness of  $76.8h^{-1}\text{Mpc}$ . The top frame shows a window of width  $102.4h^{-1}\text{Mpc}$  comoving, centered on the cluster; for clarity, only 1/2 of the mass in the viewing window is shown. The lower frame shows a magnification of a  $10.2h^{-1}\text{Mpc}$  radius circle centered on the cluster; here only 1/8 of the lowest-mass particles are shown for clarity.

ing the simulation volume is typically smaller than the filamentary structure of interest, and much smaller than the cluster radii at a fixed density contrast which we wish to estimate from the convergence maps. Furthermore, in real observations, the measured shear comes from the *gradient* in deflection angle across the image plane, and thus is related to change in the gradient of the potential across the image plane. This is small. Therefore, the error induced by integrating straight through the volume, over the unperturbed photon path, should not appreciably affect the values of the radii determined from the convergence maps.

Several interesting statistics can be drawn from a convergence map so obtained. As an example, multiplying the map by  $\Sigma_{\text{crit}}$  for the cluster and lensed source redshifts of interest transforms the map into a projected surface density map. This map can then be used to estimate  $r_{200}$ , the radius within which the mean interior density contrast is 200. In three dimensions, this radius is defined in terms of the enclosed mass by

$$M(< r_{200}) = 200 \times \left(\frac{4\pi}{3}\right) \Omega_m \rho_{\text{crit}} r_{200}^3. \quad (7)$$

A projected estimate of  $r_{200}$  is then extracted from the surface density map by considering the radius of the circle,

centered on the cluster, which contained the amount of mass given by Eq. (7) above, i.e.

$$\int_0^{2\pi} d\theta \int_0^{r_{200}} R dR \Sigma(R, \theta) = M(< r_{200}) \quad (8)$$

with  $\Sigma(R, \theta)$  the surface density on the map in terms of a two-dimensional radius  $R$ . An estimate of the radius at a density contrast of 500 can be obtained by a similar procedure. Note that this approach implicitly assumes that all the mass in the convergence map is associated with the cluster; except for lines of sight which are substantially underdense outside the cluster, this approach should result in overestimates of radii at a fixed overdensity, and thus of the mass at those radii. However, the scatter in such estimates, for different lines of sight, is driven by the dispersion in mass outside the cluster but inside a line of sight's viewing window. Unless an estimator makes an explicit attempt to correct for such contamination, the scatter in this simple projected estimate should be comparable to that in a different estimator.

The technique of aperture densitometry allows another useful quantity to be extracted from the convergence map: the so-called  $\zeta$  statistic, defined as the mean value of the convergence  $\kappa$  within a circular area on the sky of radius  $r_1$  minus the mean value within a bounding annulus  $r_1 \leq r \leq r_2$  (Fahlman et al. 1994, Kaiser 1995).

$$\zeta(r_1, r_2) = \langle \kappa(0, r_1) \rangle - \langle \kappa(r_1, r_2) \rangle. \quad (9)$$

This quantity can be written as an integral of the tangential shear  $\gamma_t$ ,

$$\zeta(r_1, r_2) = \frac{2}{1 - r_1^2/r_2^2} \int_{r_1}^{r_2} \frac{dr}{r} \langle \gamma_t \rangle, \quad (10)$$

and it is this way that the  $\zeta$  statistic is normally measured from the observational data. However, it can also be measured from mock convergence maps constructed from our data. If the mean convergence in the outer annulus is thought of as an estimate of the ‘‘background’’ contribution to  $\kappa$  everywhere, then  $\zeta$  provides an estimate of the convergence signal which comes from the cluster alone. Multiplying  $\zeta$  through by  $\Sigma_{\text{crit}}$  then gives a surface density, which can be manipulated as above to find the radius at a density contrast of 200. This, in principle, can be thought of as an attempt to correct for the projection effect we consider here; note that if the second, subtracted term in Eq. (9) were not present, the masses found from the  $\zeta$  statistic would be identically those found from Eq. (8).

Before examining each cluster and extracting such statistics, the particle dataset was cut down to a  $128 h^{-1} \text{Mpc}$  radius sphere centered on the cluster of interest. This guarantees that different lines of sight through the cluster do not include additional mass simply by geometry, by being near diagonals of the simulation cube. Since the radius of the spherical dataset is very large compared to the radii at a fixed density contrast obtained for each cluster, no significant radial surface density gradient is introduced by a decreasing chord length through the sphere with projected radius.

We observed each of the 12 clusters used from 5000 randomly chosen viewing angles, for each of the two redshifts

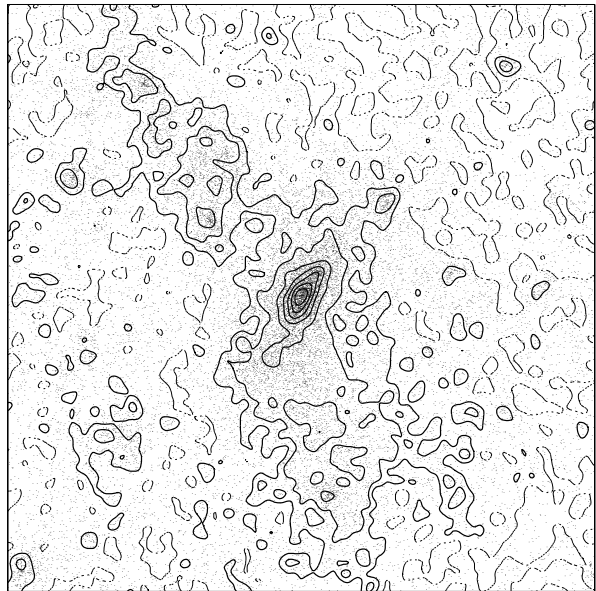


FIG. 2.— View of Cluster 6 at  $z = 0.5$  in projection through the simulation volume. The window is  $1600''$  on a side, corresponding to a linear size of  $10.3h^{-1} \text{Mpc}$  at  $z = 0.5$ . Dots represent simulation particles; only one-eighth (12.5%) of the lowest mass particles in the viewing window are shown. Contours overlaid on the plot show lines of constant convergence  $\kappa$  from the convergence map determined from the mass distribution in the viewing window. The lowest solid contour is at 0.02, while all other contours step up by 0.04 from  $\kappa = 0.04$ . The dotted line marks contours where the calculated convergence is zero, and thus denotes areas of the map which show a negative value for  $\kappa$ . This viewing angle corresponds to a mass estimate within a density contrast of 200 of  $M_{\text{lens}} = 2.7M_{\text{true}}$ .

studied. For each cluster and viewing angle, a map of the convergence  $\kappa$  was constructed using the formalism described in the previous section. To illustrate the result of this process, Fig. 2 shows a view of Cluster 6 at  $z_l = 0.5$  along one particular line of sight, along with contours showing the convergence map resulting from the procedure described in the previous section. We take the lensed sources to be at a redshift  $z_s = 1.0$  for the clusters studied at  $z_l = 0.5$ , while the sources were assumed to be at  $z_s = 1.5$  when examining the clusters at  $z_l = 1.0$ . Note that by placing the lensed sources at a fixed, known redshift, we are ignoring the potentially large source of error associated with an unknown source redshift distribution.

With the convergence map, and thus an implied surface density map, in hand, a lensing estimate of  $r_{200}$  was then obtained by determining the radius at which the mass given by Eq. 8 equals the mass inferred from Eq. 7 — that is, the radius at which the interior mass in the surface density map would be at a density contrast of 200 if contained within a sphere of that radius. This radius was compared to the cluster's true  $r_{200}$ , extracted from the three-dimensional mass distribution. The ratio of the projected mass to true mass within a density contrast of 200 is given simply by the cube of the ratio of the estimated value of  $r_{200}$  to the true, 3D value. For each cluster, a value of this ratio was obtained for each viewing angle. This process was repeated 5000 times for each cluster at each redshift. The same procedure was followed to generate values of  $r_{500}$ . The probability of encountering a particular ratio of  $M_{\text{lens}}/M_{\text{true}}$  (where by  $M_{\text{true}}$  we mean

the actual mass within a 3D radius containing the chosen overdensity) was then examined by plotting histograms of the results of this procedure.

In preparing these histograms for analysis, lines of sight producing ratios greater than 2 (i.e. estimated masses off by more than 100%) were excluded from the histograms. In many cases, such lines of sight pass through a second rich cluster, of greater mass than the one being studied. In the real universe, such a situation should be detectable through the distribution of galaxy redshifts in the viewing field; typically, the more massive cluster is likely to be the one of interest, resulting in a ratio for that cluster less than would occur for the smaller cluster. Of course, it remains possible that some lines of

sight with  $M_{\text{lens}}/M_{\text{true}} > 2$  would be produced through lines of sight which do not pass through a larger cluster, and thus would not be excluded so easily by the actual observer. However, in the spirit of making a conservative estimate of the magnitude of this effect, we uniformly exclude lines of sight with ratios so large. Furthermore, any lines of sight which pass within  $3h^{-1}\text{Mpc}$  of another rich cluster in the simulation volume, but were not caught by the “factor of 2” limit just described, were similarly excluded.

Also excluded were lines of sight which were within  $10^\circ$  of one of the principle axes of the simulation volume. The issue here is that the simulations incorporated periodic boundary conditions; along a principle axis of the box, structure at opposite ends of the line of sight through the simulation volume are correlated. Therefore, a density enhancement at one end makes a density enhancement at the other end more likely. Excluding lines of sight near the simulation volume’s principle axes reduces any spurious signal produced by the periodic boundary conditions.

#### 4. EFFECT OF STRUCTURE ON MASS ESTIMATES

##### 4.1. Measurements of $M_{200}$ at $z_l = 0.5$

We begin by considering the effect of the network of structure in which the cluster is embedded on simple estimates of the mass within a mean interior density contrast of 200. As noted above, the ratio of the estimated lensing mass within this density contrast to the actual, 3-D mass containing matter at this mean density contrast, is given by  $(r_{200,est}/r_{200,3D})^3$ , where  $r_{200,est}$  is determined from the convergence map as described above, and  $r_{200,3D}$  is determined directly from the full 3-D mass distribution. Fig. 3 shows histograms of the results of this for each cluster in the ensemble. Here the clusters were observed at a redshift of  $z_l = 0.5$ ; the lensed sources were assumed to lie at a redshift  $z_s = 1.0$ . The histograms show the resulting ratio of estimated-to-actual mass for the 5000 random viewing angles used. The clusters are ordered in the plot by their mass at this redshift, from heaviest to lightest.

Several general properties of the histograms in Fig. 3 are worth noting. First, the occasional “spiky” nature of the histograms does not come from shot noise; instead, it is due to discrete objects being inside or outside the visual field. As an example, a small halo of matter near the cluster will project entirely within the actual 3D  $r_{200}$  for a fraction of the lines of sight. For any such line of sight, the effect on the estimated value of  $r_{200}$  is identical. Second,

the histograms are strongly positively skewed, even after excluding lines of sight that are likely to generate large positive biases in the estimated mass.

The most important point to note from these histograms, however, is the magnitude of the dispersion in possible values of the mass ratio. The large dispersion is *not* induced by the anisotropic structure of the cluster itself; this was checked by regenerating the histogram for one of the clusters using a subset of the simulation particles intended to represent the cluster alone. This was done by identifying particles located at and around the cluster at local density contrasts above  $\delta = 70$  (chosen because density profiles near  $r^{-2}$  reach a local density contrast near 70 at a mean interior density contrast of 200). This set was identified as the cluster, and a small sphere containing this subset but little nearby material was then cut out of the simulation volume. The histogram produced by viewing the clearly prolate cluster at a large number of randomly chosen viewing angles produced a much narrower distribution, with a maximum offset of less than 10% in the mass ratio and a mean offset of approximately half that value.

We will see in §7.2 that the mean values of the histograms are driven by material within 20 Mpc of the cluster; material outside this distance serves primarily to widen the dispersion in possible values of  $M_{\text{lens}}/M_{\text{true}}$  resulting from an observation. While the mass estimator used herein is simplistic, and by construction was expected to produce a positive bias in the mass estimate, any estimator which might correct for such bias (by, for instance, assuming a model for the radial distribution of matter outside clusters) will still run afoul of this large dispersion. Large discrepancies between the weak lensing mass and the virial mass of clusters are possible.

To illustrate using another mass estimator, in Fig. 4, we show aperture densitometry plots for Cluster 6, for five lines of sight through the cluster. The lines of sight were chosen to span a range in  $M_{\text{lens}}/M_{\text{true}}$  from the simple projected estimator of from 1.0 to 2.0. We have taken an outer radius of  $\theta_2 = 800''$ , within the half-degree field of view typical of new large CCD cameras. We have explicitly checked that reducing the radius to half this value does not change our result. Also shown are two curves marking the value required of  $\zeta$  at a given radius for that radius to enclose a given estimated density contrast. For example, where a particular  $\zeta$  profile crosses the line labelled “200” marks the radius that aperture densitometry would suggest is  $r_{200}$  for that line of sight. If a  $\zeta$  profile lies above that curve, the mean interior density contrast at that radius is higher than 200, while below implies lower than 200. Amongst the lines of sight shown, the largest estimated  $r_{200}$  is a factor of 1.18 larger than the smallest, corresponding to a factor of 1.63 difference in mass; this should be compared to the factor of two difference between largest and smallest masses predicted by the simple projected estimator. Thus, the masses predicted from aperture densitometry appear to have a dispersion tighter than given by simple projected mass estimates, but still quite substantial; such techniques as aperture densitometry can ameliorate our problem, but do not resolve it. None of the curves shown clearly indicate anything untoward about the line of sight shown; an observer would not be driven to suspect a strong bias in the estimated mass from the shape of the  $\zeta$  profile even in the most extreme

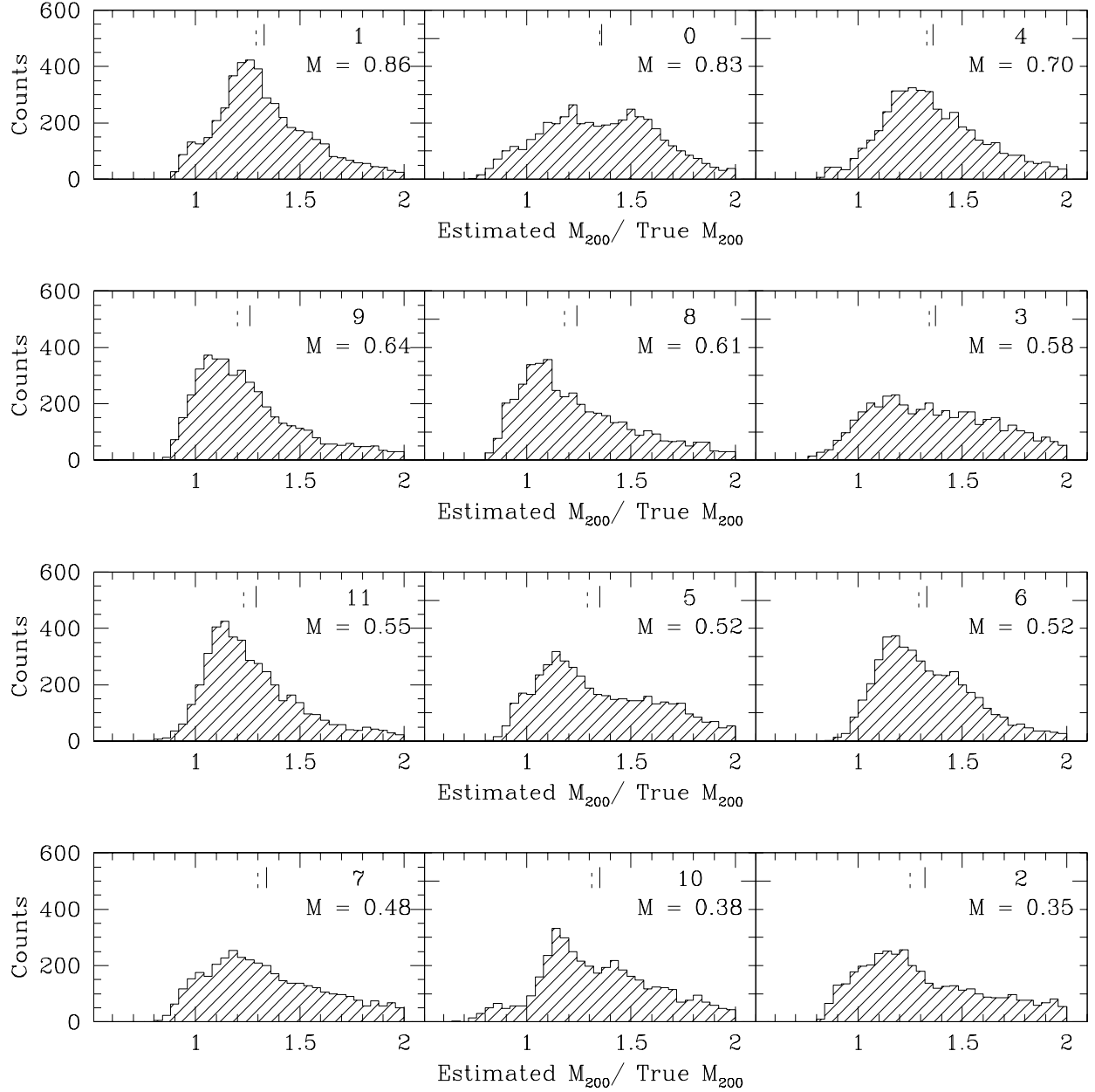


FIG. 3.— Histograms of  $M_{\text{lens}}/M_{\text{true}}$ , measured within a mean interior density contrast  $\bar{\delta} = 200$ , at  $z=0.5$ . Clusters are ordered by  $M_{\text{true}}$ , with the mass given for each cluster in units of  $10^{15} M_{\odot}$ . Lines of sight near the box principle axes, through identified large clusters, or producing mass estimates twice that of the cluster, are all excluded. The vertical hash mark near the top of each box indicates the location of the mean for that cluster's histogram.

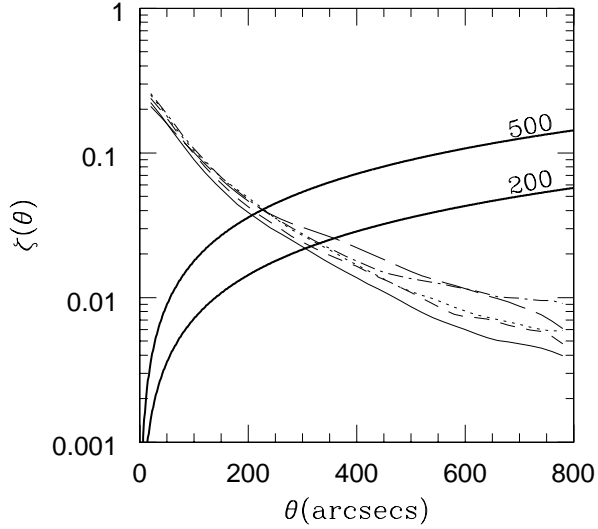


FIG. 4.— Aperture densitometry plot for one cluster (6), showing  $\zeta$ -profiles for five lines of sight, as well as curves which mark the value of  $\zeta$  at a given radius for a mean interior density contrast of 200 or 500. Here  $\theta$  defines the inner radius of the aperture used for each point, with the outer radius at  $800''$ . The lines of sight used were chosen because the simple projected estimator, applied to each line of sight, returned a value of 1.00 (solid), 1.25 (dotted), 1.50 (short dashed), 1.75 (long dashed), and 2.00 (dot-dashed).

cases shown here.

The histograms in Fig. 3 were used to construct a cumulative probability distribution function for the possible values of  $M_{\text{Iens}}/M_{\text{true}}$ . A plot of the PDF is shown in Fig. 5. Also shown is a simple approximation to the shape of the PDF with a smooth curve. As there is no theoretical prejudice in favor of any particular shape for the curve used, a simple approximation using polynomials was constructed by hand, for use later in §5. It errs on the conservative side, in that the strength of the effect predicted by the smooth curves is less than is actually seen in the simulated data; the mean of the curve shown is 1.28 with a dispersion of 0.23, in contrast to the actual data which show a mean of 1.32 and a dispersion of 0.26. This is again in the spirit of suggesting a conservative lower bound for the size of the effect in §5.

#### 4.2. Measuring masses at higher density contrast

Note that in Fig. 4, the dispersion in estimated values of  $r_{500}$  is much tighter for the lines of sight shown. This suggests that measuring masses within a higher mean interior density contrast reduces the magnitude of this effect. Fig. 6 repeats the exercise in constructing Fig. 3, but with measuring the estimated and actual mass within a density contrast of 500.

From these histograms, it does not appear that any such reduction in the magnitude of the dispersion occurs. The mean for the cumulative PDF of these histograms is 1.44, much larger than the mean of 1.32 found for the  $r_{200}$  histograms; the standard deviation is 0.23, only slightly (but statistically significantly) smaller than for the  $r_{200}$  case. There appears to be little reduction in dispersion, and no reduction in bias, by going to  $r_{500}$  with the simple pro-

jected estimator. The reason behind not seeing any reduction in the bias here, yet apparently seeing such a reduction in the predictions of the lines of sight examined in Fig. 4, is likely attributable to the effect of subtracting the outer annular mean of the convergence in constructing  $\zeta$ . Without this term in the definition of  $\zeta$  — if  $\zeta$  were defined solely by the average  $\kappa$  within a given radius — then the masses thus calculated would be simply a product of the surface area within that radius and  $\zeta$ , the average value of the convergence. This is identically the same process as is used to find Fig. 4. Therefore, the decrease in dispersion must be from subtracting off the outer annulus. In other words, whether measuring masses at a higher density contrast reduces the magnitude of the dispersion appears to depend on the estimator used; determining the dispersion of a proposed estimator through methods such as used here is important for understanding the results of the estimator.

Previously, studies of the accuracy of cluster X-ray binding mass estimates showed that such estimates were much more robust when measured within a mean interior density contrast of  $\bar{\delta} = 500$  than when  $\bar{\delta} = 200$  was used, for reasons related to the dynamical and thermodynamic state of the intracluster gas (Evrard, Metzler & Navarro 1996). It is somewhat surprising that no comparable result appears here. Since the means of the histograms displayed in Fig. 3 show range from 1.24 to 1.37, it is quite possible that sample variance plays a role here.

#### 4.3. Evolution with redshift

Also of interest is how the evolution of structure affects the magnitude of this effect. We might expect the contamination by projected structure to be *worse* for clusters at higher redshift. Consider a cluster at  $z = 0.5$  from a particular line of sight. As the cluster evolved from  $z = 1.0$  to  $z = 0.5$ , the amount of projected mass within a  $40'$  field of view likely changed little. What changed, instead,

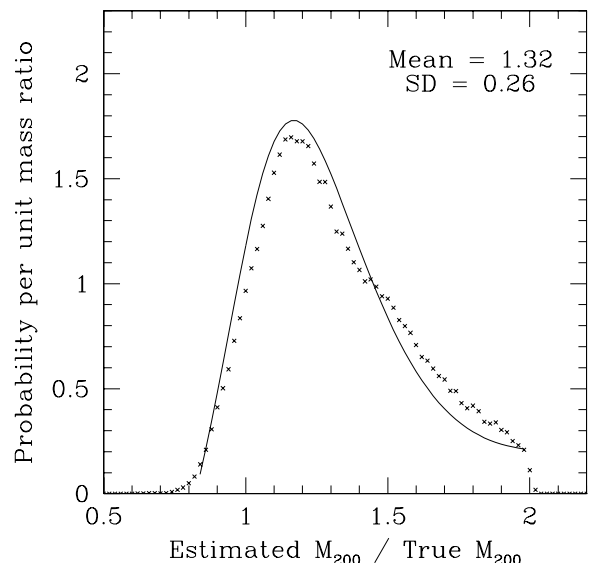


FIG. 5.— A PDF of  $M_{\text{Iens}}/M_{\text{true}}$  for the ensemble at  $z = 0.5$ . The points mark the PDF as derived from the ensemble, while the solid curve shows an intentionally conservative polynomial approximation to the data.

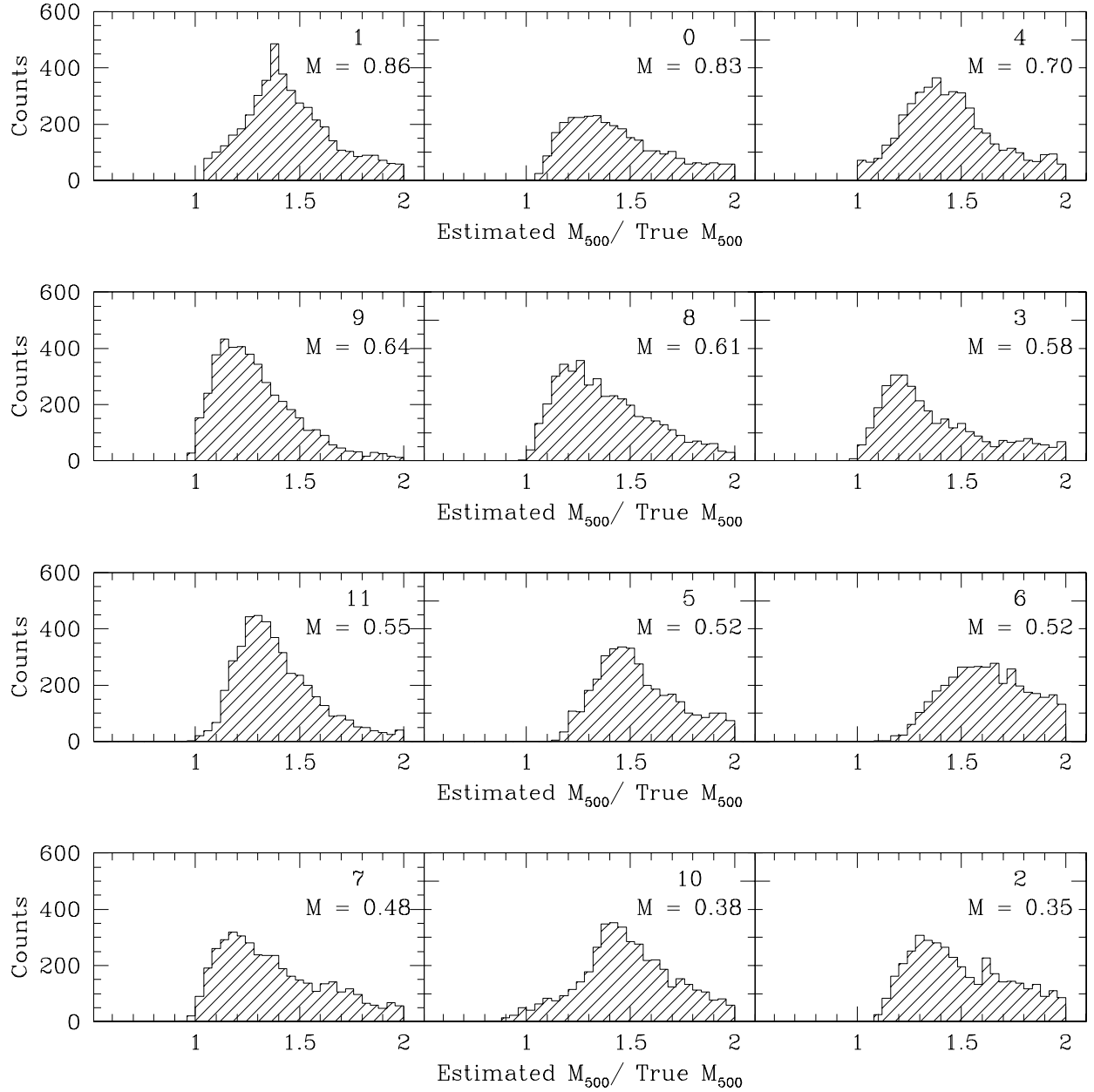


FIG. 6.— Histograms of  $M_{\text{lens}}/M_{\text{true}}$ , measured within a mean interior density contrast  $\bar{\delta} = 500$ , at  $z=0.5$ . Clusters are ordered by  $M_{\text{true}}$ , with the mass given for each cluster in units of  $10^{15} M_{\odot}$ .

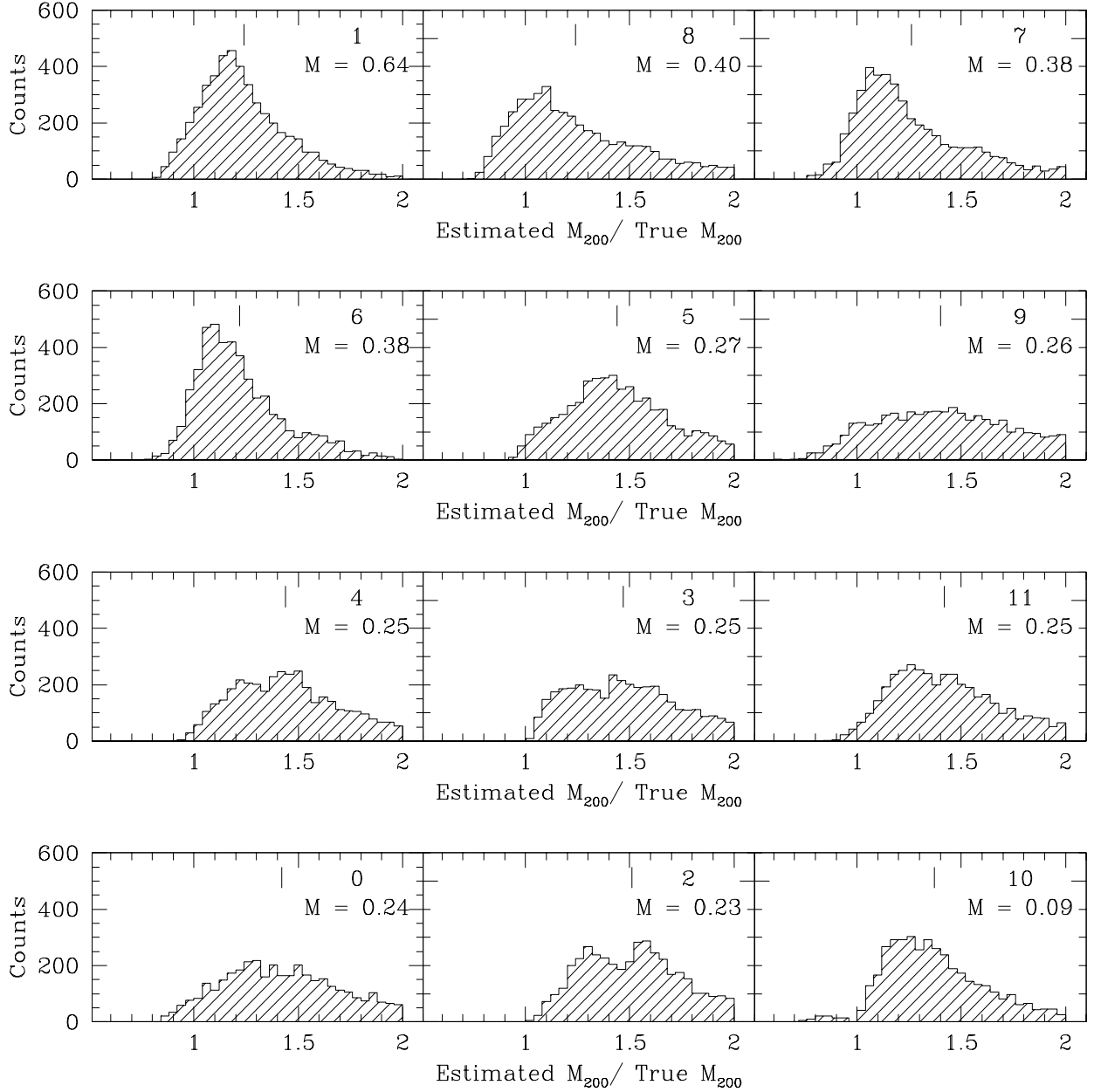


FIG. 7.— Histograms of  $M_{\text{ens}}/M_{\text{true}}$ , measured within a mean interior density contrast  $\bar{\delta} = 200$ , at  $z=1.0$ . Clusters are ordered by  $M_{\text{true}}$ , with the mass given for each cluster in units of  $10^{15} M_{\odot}$ . Lines of sight near the box principle axes, through identified large clusters, or producing mass estimates twice that of the cluster, are all excluded. The vertical hash mark near the top of each box indicates the location of the mean for that cluster's histogram.

was the amount of this mass contained within the cluster of interest, and the amount contained in smaller halos and nearby filamentary structure that merged with the cluster in the intervening time. Thus, large clusters with a small amount of foreground and background material (and thus a small effect on the mass estimate) at  $z = 0.5$  were likely smaller clusters with a somewhat larger amount of foreground and background material (and thus a larger effect on the mass estimate) at  $z = 1.0$ .

Fig. 7 shows the  $M_{\text{lens}}/M_{\text{true}}$  histograms for  $M_{200}$  estimated for the clusters at  $z = 1.0$ . Again, the clusters are ordered by their mass at that redshift, with the mass in units of  $10^{15}M_{\odot}$  shown, and a vertical hash mark denoting the mean of each histogram. By eye, for most clusters, both the means and the dispersions are consistently larger than their counterparts at  $z = 0.5$ . This is not always true; Cluster 6 is an exception to this rule. A coadded histogram of the  $z = 1.0$  data yields a mean and dispersion of 1.36 and 0.27, compared to 1.32 and 0.26 at  $z = 0.5$ . The effect is not large but, coming from 5000 lines of sight, is statistically significant; for instance, the difference between the two means is significantly larger than the uncertainties in their values. Thus, while we continue our analysis using the  $z = 0.5$  dataset, to be conservative about the magnitude of this effect, it should be noted that the problem is likely worse for clusters at still higher redshift.

##### 5. LIKELIHOOD OF CLUSTER ACTUAL MASS GIVEN AN OBSERVED ESTIMATE

In the previous section, we considered the distribution of possible values of the ratio  $M_{\text{lens}}/M_{\text{true}}$  — that is, the distribution of possible observational estimates for the mass of a cluster given its true mass within the density contrast of interest. In the real universe, however, the problem faced by an observer is the opposite: given an estimate of the mass taken from observations, what might the actual mass of the cluster be? The histograms we examined in the previous section give us the probability of observing a certain lensing mass given a certain true mass,  $P(M_{\text{lens}}|M_{\text{true}})$ ; in real situations, we typically desire the the inverse quantity, the likelihood of a true mass of a given value, given an observed lensing mass,  $P(M_{\text{true}}|M_{\text{lens}})$ .

We can examine this by considering clusters with an observed mass  $M_{\text{lens}}$ . If the probability of a cluster with a true mass  $M$  being observed with mass  $M_{\text{lens}}$  is given by  $P(M_{\text{lens}}|M)$ , and if the *number density* of clusters with true mass in the range  $(M, M + dM)$  is given by  $n(M) dM$ , then the product  $P(M_{\text{lens}}|M) n(M) dM$  gives the number density of clusters with true masses in the range  $(M, M + dM)$  which are then observed to have an effective lensing mass  $M_{\text{lens}}$ . Since the total number density of clusters with observed mass  $M_{\text{lens}}$  should be given by an integral of this function, we can find the likelihood of interest by forming the fraction. In other words,

$$\frac{\int_{M_1}^{M_2} P(M_{\text{lens}}|M) n(M) dM}{\int_0^{\infty} P(M_{\text{lens}}|M) n(M) dM} \quad (11)$$

gives the probability that a cluster with an observed lensing mass  $M_{\text{lens}}$  has an actual mass in the range  $(M_1, M_2)$ .

We can understand the qualitative nature of the effect by examining the terms of the integral in the numerator. In the previous section, we noted the biased form of the

$M_{\text{lens}}/M_{\text{true}}$  distribution; this argues that observed masses are likely overestimates of the true mass of a cluster. One can imagine that this bias could be corrected for, using an estimator that takes contamination of the mass estimate by foreground and background mass into account. This would remove such a bias, but not the distribution of the scatter about the mean.

However, we must also consider the effect of the cluster mass function,  $n(M) dM$ , the number density of clusters as a function of mass. Theory and observations both strongly suggest that this is a steeply falling function with mass; there are more low mass clusters than there are high mass clusters. Because of this, even if the distribution of observed lensing masses  $P(M_{\text{lens}}|M_{\text{true}})$  from the previous section were symmetric about the mean — even if there were no bias in the mass estimator — it would still be more likely to overestimate masses than underestimate them. To explain this in more concrete terms, consider a cluster with an observed lensing mass  $M_{\text{lens}} = 10^{15}M_{\odot}$ . If we consider two values of the actual cluster mass  $M_1 = 8.33 \times 10^{14}M_{\odot}$  and  $M_2 = 1.25 \times 10^{15}M_{\odot}$  (mass ratios  $M_{\text{lens}}/M_{\text{true}}$  of 1.2 and 0.8 respectively), then even if the probability that clusters of masses  $M_1$  and  $M_2$  will be observed at lensing mass  $M_{\text{lens}}$  is the same (as would be the case if our histograms were unbiased and symmetric), it is still more likely that a given cluster observed at  $M_{\text{lens}}$  has mass  $M_1$  than  $M_2$ , simply because there *are more clusters* at mass  $M_1$  than  $M_2$ .

Thus, *we expect that weak lensing masses for clusters systematically overestimate the true masses of clusters within the density contrast of interest.* To be fair, this effect should occur with any mass estimator, whether based on lensing, hydrostatic, or dynamical arguments since any estimator is bound to have some scatter in its predictions. The magnitude of the overestimate is dependent on two things: the width of the distribution  $P(M_{\text{lens}}|M_{\text{true}})$ , which for weak lensing we considered in the previous section; and the steepness of the mass function at the observed value  $M_{\text{lens}}$ . The massive clusters ( $M_{200} \simeq 10^{15}M_{\odot}$ ) at moderate redshift that provide the typical objects for weak lensing analysis lie on or near the exponential cutoff of the theoretical Press–Schechter mass function; the magnitude of these overestimates can be expected to be quite strong.

In Fig. 8, we show the likelihood that a cluster at  $z = 0.5$ , observed to have a lensing mass within a density contrast of 200 of either  $M_{\text{lens}} = 5 \times 10^{14}M_{\odot}$  or  $10^{15}M_{\odot}$ , has an actual mass within a density contrast of 200 equal to or greater than  $M$ . To construct this figure, the theoretical Press–Schechter mass function for the  $\Lambda$ CDM model assumed in this paper was used. Several different curves relating possible values of the observed mass to the true mass were considered. For the lensing mass, the curves shown indicate that it is 100% likely that the actual cluster mass is greater than half the observed mass; this merely reflects the fact that in constructing  $P(M_{\text{lens}}|M_{\text{true}})$ , we artificially truncated the error histograms at  $M_{\text{lens}}/M_{\text{true}} = 2$ , as explained earlier. The important point to take from this plot is that regardless of the magnitude of the dispersion, it is unlikely that the cluster actually has the observed mass or greater. Even without a bias, a dispersion of 30% in the mass ratios indicate that a cluster observed at a mass of  $5 \times 10^{14}M_{\odot}$  is 70% likely to be of lower mass, while a

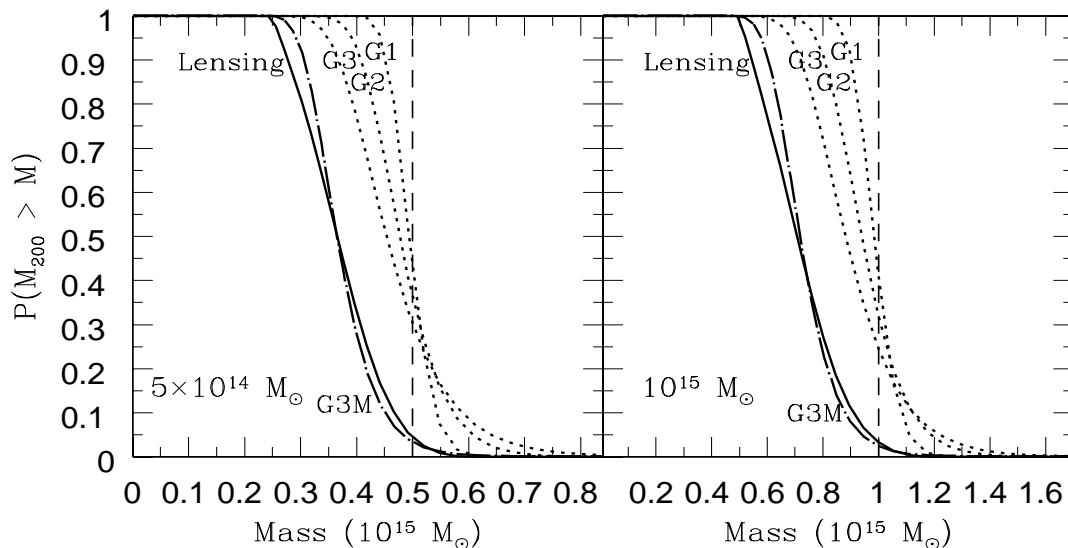


FIG. 8.— The likelihood that a cluster with an observed lensing mass within  $\bar{\delta} = 200$  of  $M_{\text{lens}} = 5 \times 10^{14} M_{\odot}$  (left) or  $M_{\text{lens}} = 10^{15} M_{\odot}$  (right) has an actual mass within  $\bar{\delta} = 200$  greater than or equal to  $M$ , at  $z = 0.5$ . The observed  $M_{\text{lens}}$  is marked by a dashed line. Considered are six possible PDFs mapping the probability of finding a particular observed mass given an actual mass. The heavy solid line to the left in each case shows the likelihood curve for the PDF we derived in Fig. 5. The three dotted curves marked G1, G2, and G3 show the result for Gaussian PDFs in the mass ratio centered on  $M_{\text{lens}}/M_{\text{true}} = 1$ , with dispersions of 0.1, 0.2, and 0.3 respectively. The dot-dashed curve marked G3M shows the result for a Gaussian PDF with a dispersion of 0.3, but with the mean ratio shifted to 1.3, comparable to that of the PDF in Fig. 5.

cluster at  $10^{15}$  is over 75% likely to be of lower mass. The situation is far worse if the dispersion is larger or if a bias exists.

## 6. THE MASS FUNCTION

If there is some dispersion in possible observed masses for clusters — that is, if the mapping from actual mass to observed mass is not one-to-one — then there will also be an effect on the observed mass function. The number density of clusters of some observed mass  $M_{\text{lens}}$  will actually be comprised of contributions from a range of actual cluster masses. This can be described by a convolution of the true mass function with the probability of observing a cluster of mass  $M_{\text{true}}$  at a given mass  $M_{\text{lens}}$ . Mathematically, the abundance of clusters with observed masses in the range  $(M_{\text{lens}}, M_{\text{lens}} + dM_{\text{lens}})$  should be given by

$$n(M_{\text{lens}}) dM_{\text{lens}} = dM_{\text{lens}} \int_0^{\infty} P(M_{\text{lens}}|M_{\text{true}}) n(M_{\text{true}}) dM_{\text{true}} \quad (12)$$

where, as earlier,  $P(M_{\text{lens}}|M_{\text{true}})$  is the probability that a cluster with an actual mass of  $M_{\text{true}}$  will be observed with mass  $M_{\text{lens}}$ . Fig. 9 demonstrates the result of this convolution, using the PDF derived for Fig. 5. Here an extra integral is done, from a given mass to infinity, to find the number density of clusters above a given mass. Plotted are both the expectation for the number density above a given observed mass value  $M_{\text{lens}}$  (dashed line) and the number density above a given actual mass  $M_{\text{true}}$ . The figure suggests that lensing observations would indicate three times as many clusters at a mass of  $10^{15} M_{\odot}$  as are

actually present. This is significant, but certainly insufficient to mimic the lack of strong evolution at the high end of the mass function argued by e.g. Bahcall & Fan (1998).

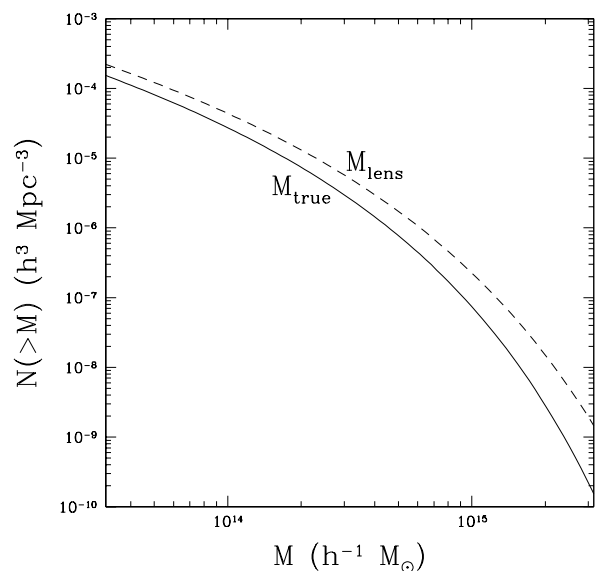


FIG. 9.— The number density of clusters predicted to lie above a given mass  $M$ . The solid line indicates the actual mass function predicted by Press-Schechter, while the dashed line indicates the abundance as a function of observed  $M_{\text{lens}}$ .

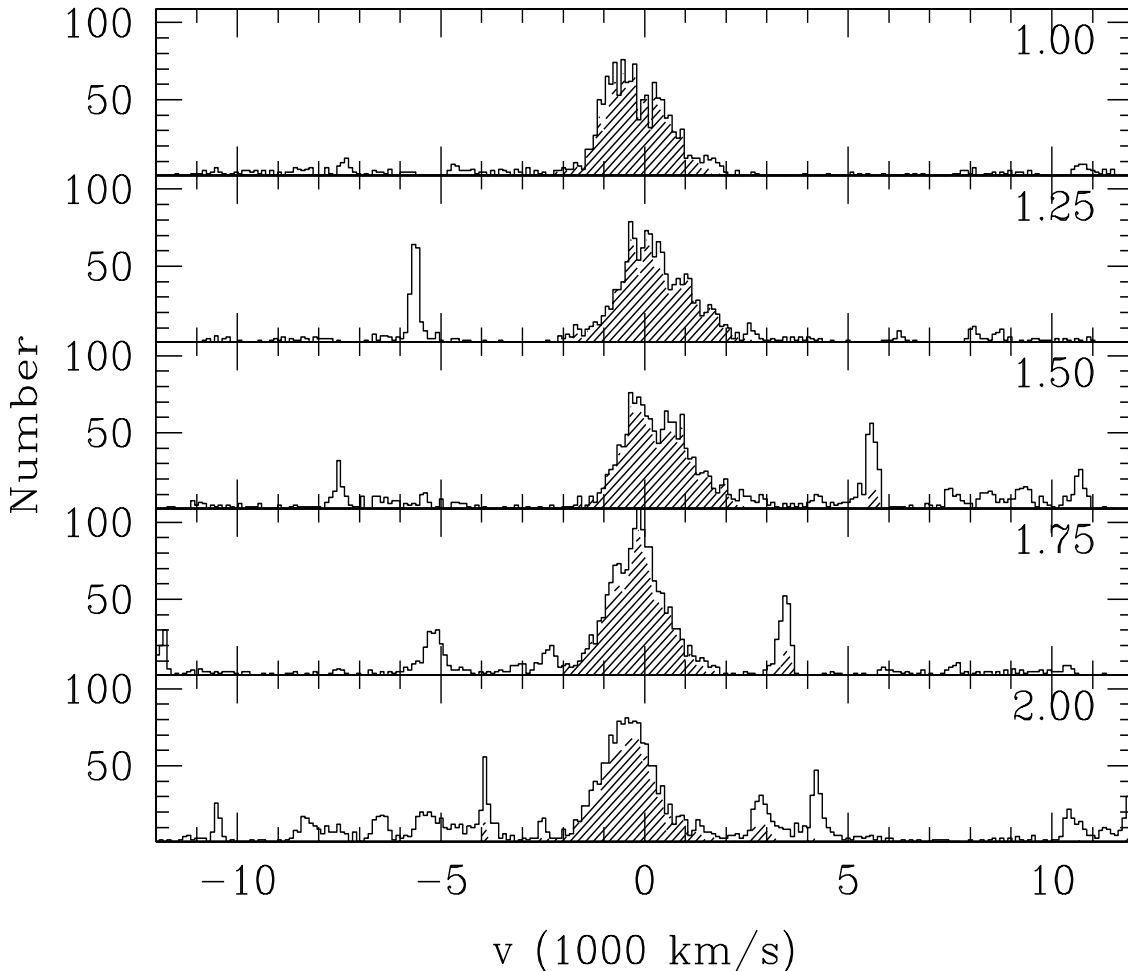


FIG. 10.— Line of sight velocity histograms for the five lines of sight through Cluster 6 previously examined in Fig. 4; numbers in the upper right-hand corner indicate the mass ratios associated with each line of sight, for the simple projected estimator. Material used in forming the histograms was taken from a viewing “cylinder” of radius  $3h^{-1}\text{Mpc}$ ; the space between tick marks in the plot corresponds to  $1000\text{ km/s} = 10h^{-1}\text{Mpc}$ , and thus a volume associated with each tick mark of  $283h^{-3}\text{Mpc}^3$ . The unshaded outline shows the histogram produced by the mass in the line of sight, while the shaded subset of the histogram is produced by mass at density contrasts above 50.

## 7. DISCUSSION

### 7.1. Detecting projection effects with line of sight velocities

One way in which an observer might hope to avoid being fooled by this sort of projection effect is by examining line of sight velocities of galaxies. If a velocity histogram suggests a clump of mass in the foreground or background of the cluster, an observer could assume that a lensing mass measurement from this cluster would be corrupted. While this would not remove the effect on mass measurements of this cluster, it would remove the cluster from consideration, and thus avoid any false scientific conclusions drawn from an incorrect mass assigned to this cluster. For instance, ignoring a mass estimate from a cluster which clearly has a strong foreground or background mass concentration would then reduce the chance of overestimating the abundance of high-mass clusters.

In constructing the histograms shown earlier, we as-

sumed that an observer would be perfectly able to avoid such lines of sight when we explicitly excluded lines of sight which pass through another large cluster in the volume. Thus, the histograms at present have attempted to correct for foreground and background contamination by other objects. However, it is still worth considering whether galaxy redshifts could help us to exclude cases where no big objects such as rich clusters ruin our measurement, but instead a filament is oriented near or across the line of sight.

The simulations used for this project do not model galaxy formation. Indeed, in the lowest resolution region (outside the cluster environs, and comprising most of the volume of the simulation), individual collisionless particles have masses  $\sim 6.66 \times 10^{11}h^{-1}M_{\odot}$ , so approximating galaxies by halos is not available to us. Instead, we tie galaxy locations to the background overdensity field, and consider two scenarios: a simple model where galaxies trace the mass along the line of sight; and a model where

galaxies are biased tracers of the mass, lying in regions where the mean local density contrast is above 50.

Fig. 10 shows the results of this process. Here we have taken five lines of sight through Cluster 6, corresponding to  $M_{\text{lens}}/M_{\text{true}}$  values of 1.0 – 2.0 which were not excluded in making the cluster histogram as no large lumps exist in the cluster foreground or background. These correspond to the same lines of sight used in Fig. 4. For each, a line-of-sight velocity histogram was constructed by considering particles taken from the overall mass distribution and its velocity field. Shown within that histogram is a smaller shaded one, detailing the histogram produced by matter at density contrasts of 50 or higher.

The velocity histograms determined by the full mass distribution shows that if galaxies trace the mass, one cannot generically count on line-of-sight velocities to veto cases with large errors, even when densely sampled. The last example shown here — a line of sight towards Cluster 6 producing an error in the mass estimate of a factor of 2 — is driven by comparatively diffuse mass extending over a range of radii in the foreground: a filament of mass. It is not at all clear that a histogram of galaxy velocities would pick this up. Note in the line of sight with mass ratio 1.25 shown here, a mass concentration 50–60 $h^{-1}$ Mpc in the foreground corresponds to a filament cutting *across* our line of sight, rather than to any one specific collapsed object.

The situation is even worse if galaxies are expected to lie preferentially in regions of high overdensity. As noted, the shaded area indicates a histogram drawn from regions with overdensity greater than 50; the difference between this histogram and the parent (unshaded) histogram highlights the difference between the expected sort of histograms should galaxies trace the mass directly and should galaxies be biased towards higher-density regions. In the latter case, it is quite clear that clumps of galaxies in a line of sight velocity diagram cannot be counted upon to screen out any potentially large errors.

### 7.2. Scale dependence of results

In studying the magnitude of this effect, we have been considering matter contained within spheres of radius 128 $h^{-1}$ Mpc centered on the cluster of interest. Of course, in the real universe, when observing a cluster along a particular line of sight, there exists material at distances greater than 128 $h^{-1}$ Mpc away from the cluster — material in the foreground, between us and the cluster lens, and in the background between the lens and the source, but further away from the cluster than 128 $h^{-1}$ Mpc. What effect should this material have on the estimated lensing mass?

To examine this, we repeated the procedure used in constructing Fig. 3 for Cluster 6 several times; however, instead of using the full simulation dataset (a sphere of radius 128 $h^{-1}$ Mpc centered on the cluster), we used datasets centered on the cluster but cut off at a different radius each time. This allows study of the evolution of the histogram as a function of the volume of matter around the cluster being considered in calculating the effect. In particular, we considered the first four moments of the histogram for Cluster 6 at  $z_l = 0.5$ ; the results of this analysis are shown in Fig. 11. Each radial point corresponds to taking a sphere of material of that radius, centered on the cluster, and using 5000 lines of sight through that sphere to

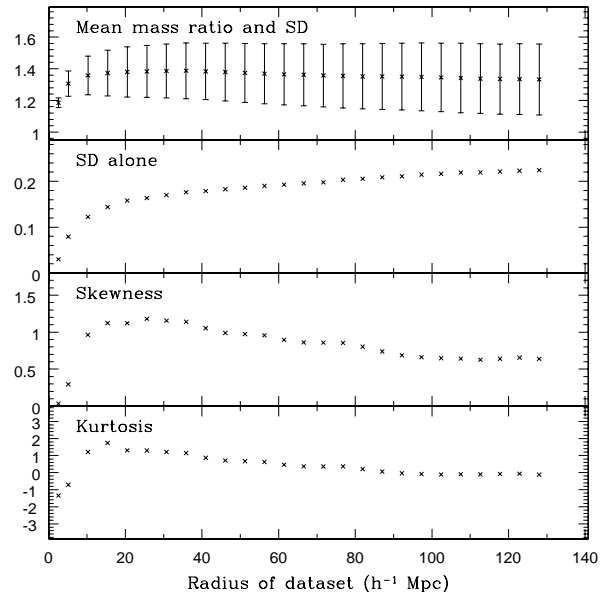


FIG. 11.— Moments of the distribution of  $M_{\text{lens}}/M_{\text{true}}$  for Cluster 6, as a function of the outer radius of the particle dataset used to calculate the distribution. The data points showing the moments for the largest radius distribution correspond to using the full simulation dataset, and thus are the moments of the histogram for Cluster 6 shown in Fig. 3.

determine the moments of the distribution of  $M_{\text{lens}}/M_{\text{true}}$ . The last data points for each moment, at a radius of 128 $h^{-1}$ Mpc (half the box size), corresponds to the histogram for Cluster 6 shown in Fig. 3. The most striking feature to note is that the mean value of the histogram is reached at comparatively small radii for the dataset. The mean error is driven primarily by material within 10 – 20 Mpc of the cluster. As the radius of the dataset used decreases, the histogram converges towards that driven by the asymmetry of the cluster itself. Also, the *shape* of the histogram appears to have converged; the skewness and kurtosis of the histogram for material with 100 $h^{-1}$ Mpc remains relatively unchanged after considering the effects of material at still larger radii.

The standard deviation of the histogram, on the other hand, appears to still be increasing as the effect of material further and further away from the cluster is considered. One plausible interpretation of this result is as follows. When only the material within a sphere of a given radius is considered, a line of sight through the cluster will produce some lensing mass estimate. Considering a slightly larger sphere of material will slightly change the estimate produced along each line of sight, by an amount dependent upon the overdensity contained within the small additional segment of volume that lies along the line of sight. Thus, the new histogram of this larger sphere can be thought of as the histogram describing the smaller sphere *convolved* with a function dependent upon the distribution of overdensities expected in these volumes. Therefore, at a large enough radius from the cluster, this component should simply be noise uncorrelated with the cluster itself; the result is to broaden the histogram, resulting in an increasing second moment. This was checked by plotting the mass

estimates arising from the material within a given large radius (e.g.  $123h^{-1}\text{Mpc}$ , the second-to-last points in radius on Fig. 11) with the *change* in the mass estimate when all the material (out to  $128h^{-1}\text{Mpc}$ , the last point in Fig. 11) is used. The result was no appreciable correlation, with a correlation coefficient of  $r = 0.10$ .

### 7.3. Comparison With Other Work

Papers by Cen (1997), Reblinsky & Bartelmann (1999) and Brainerd *et.al.* (1999) have previously examined the accuracy of weak lensing mass estimates.

Cen (1997) constructed mock surface density maps by simply projecting down the mass in the simulation, subtracting off a constant background since matter at the background density does not contribute to the lensing signal. In the limit of no variation of the lensing kernel in Eq. (5), these approaches should be equivalent. Cen reported substantially smaller positive bias in the lensing mass than we have seen here, typically of only 5–10%. On the surface, this appears to be discrepant with our result.

However, masses compared by Cen were measured within an aperture of fixed size, rather than an aperture whose size depends on the mass within, as we use here. Furthermore, the magnitude of the bias seen by Cen depended strongly on the size of the aperture used, and increased dramatically between apertures of radii  $1h^{-1}\text{Mpc}$  (a median value of just under 14%, by eye from Fig. 19) and  $2h^{-1}\text{Mpc}$  (approximately 40%). Cen measured the bias and dispersion of  $M_{lens}/M_{200}$  using an aperture for each cluster equal to its three-dimensional value of  $r_{200}$ , and found results substantially similar to those for a fixed aperture of  $1h^{-1}\text{Mpc}$ . This suggests that  $1h^{-1}\text{Mpc}$  is representative of the  $r_{200}$  values for the 50 clusters in Cen’s sample, which was taken at  $z = 0$ . The 12 clusters in our sample represent the high-mass tail of the cluster mass function, in a box 8 times as large; the values of  $r_{200}$  represented at  $z = 0.5$  range from  $1.01h^{-1}\text{Mpc}$  to  $1.54h^{-1}\text{Mpc}$ . The median value for the bias we obtain using a fixed aperture for each cluster equal to that cluster’s 3D value of  $r_{200}$ , similar to Cen, is 24%; the median using a fixed aperture of  $2h^{-1}\text{Mpc}$  is 1.56. We believe the difference in the magnitude of the bias seen by Cen and ourselves lies in the different cluster samples used — Cen’s sample running much further down the mass function — and also in sample variance. With regard to the latter, the medians for the mass ratios obtained from each cluster independently, using a  $2h^{-1}\text{Mpc}$  fixed aperture, range from 1.38 to 1.85.

We emphasize again that the dispersion in measured values of the mass is the important quantity from Fig. 5, since any attempt by an estimator to correct for any bias from projected material must still contend with the variance in the amount of projected material along different lines of sight. Fig. 19 of Cen (1997) suggests approximately 6% of his cluster lines of sight have mass ratios  $M_{lens}/M_{200}$  measured within the 3D  $r_{200}$  with values above 1.58; with our smaller, larger mass sample, we see 10% of our lines of sight above this value. For a fixed projection aperture of  $2h^{-1}\text{Mpc}$ , Cen sees 10% of his cluster observations yielding mass ratios in excess of approximately 2.0; we see 10% lying above 2.14. Within the limits of sample variance, we do not believe our results on the dispersion are significantly different from Cen. In any case, both our work and

Cen (1997) imply that large values of the mass ratio are not uncommon.

In Reblinsky & Bartelmann (1999), mock shear maps of simulated clusters were obtained by first projecting the mass into two-dimensions to construct the convergence, then solving the Poisson equation for the 2D lensing potential, Eq. 2, and finally taking the appropriate derivatives to find the complex shear. The tangential shear was then used to find the  $\zeta$ -parameter using Eq. 10. Finally, the system of equations relating  $\zeta(r_1, r_2)$  (for a range of values of  $r_1$  out to  $r_2$ ) and the appropriate averages of the convergence  $\kappa$  (see Eq. 9) were solved for the mass profile assuming no convergence in the outermost annulus. These masses were then compared to the 3D mass, using  $r_{3D} = r_2 = 1.8h^{-1}\text{Mpc}$ . While on the surface their results appear consistent with ours — means, medians and dispersions which are roughly comparable to those presented here — the comparison is in fact difficult to make directly. The mass range of the cluster sample used by Reblinsky & Bartelmann lies a factor of 4–10 lower than that used here. Their positive bias in  $M_{lens}$  is driven by their lowest-mass cluster; higher mass systems appear to evidence a trend towards *underestimating* masses. However, their setting the effective convergence to be zero at  $1.8h^{-1}\text{Mpc}$  can be interpreted as estimating the typical foreground/background mass contamination and subtracting that off; different mass estimators can be expected to have different means, or degrees of bias. The important comparison to be made is the dispersion in their mass ratios, 0.34, which actually exceeds that in our sample and appears relatively insensitive of the subsample taken. The apparent trend in their sample of decreasing bias with larger mass systems is not seen in our sample, although it was seen in our previous letter (Metzler *et al.* 1999). Given the sample-dependence of this trend in our work, and that the trend seems much less prominent in the dataset of Reblinsky & Bartelmann when restricted to the highest-mass clusters more akin to our ensemble, the reality of this trend is unclear.

In Brainerd *et.al.* (1999), shear maps were constructed by explicit ray-tracing through the volume of interest. Estimated lensing mass profiles were then derived from the shear maps by assuming that the simulated cluster was a singular isothermal sphere, in which case the cluster velocity dispersion (and thus the mass profile) is a simple function of the average shear over an annulus. Brainerd *et.al.* found quite good agreement between their estimated lensing masses and the actual cluster masses — the lensing masses typically being 5–10% underestimates (*cf.* the outermost circle-points in their Fig. 9). However, their shear maps were constructed using only the matter on their highest-resolution grid within their clusters’ true, three-dimensional value of  $r_{200}$ ; the effect of structure at larger distances from the cluster is not considered at all. In other words, Brainerd *et.al.* probed primarily the effect of the anisotropic shape of the cluster itself, which we agree (as noted above) has a small effect on mass estimates. However, their study is not sensitive to the effect of the large-scale structure in which the cluster is embedded, examined here.

In this paper, we have examined how weak lensing mass estimates of galaxy clusters are affected by the large-scale structure in which the clusters are embedded. We find that cluster masses are typically overestimated, with mean errors of tens of percent for clusters at redshifts  $z \simeq 0.5$ , although the exact value depends on the mass estimator chosen; any mass estimator used on real observations should be calibrated through methods such as described here. These errors are likely worse for clusters at higher redshift ( $z \simeq 1.0$ ). We also note that as long as there exists a dispersion in observed masses possible for a given actual mass (e.g. along different lines of sight through the cluster), *even an unbiased estimator* is likely to produce observed mass estimates which are systematically higher than the actual virial masses of clusters; this is simply because there are more low-mass clusters which can be erroneously assigned a high mass than there are high-mass clusters which can be erroneously assigned a low mass. The magnitude of this effect is crucially dependent on the estimator used and should be considered carefully when implementing a particular estimator. Such approaches as simple projection and aperture densitometry do not appear to perform better than simple virial estimates based on cluster X-ray temperatures alone, although temperature-based estimates suffer from calibration uncertainties that would induce a bias if unresolved. The effects of large-scale structure examined here are not typically resolved through the examination of galaxy redshifts in the viewing field.

The authors would like to thank Chris Kochanek and Ludovic van Waerbeke for useful discussions, Mike Norman for his assistance in using the LCA/MARG X-ray Cluster Archive, and our referee for several valuable suggestions. This research was supported by the National Science Foundation under grant number PHY-0096151.

## REFERENCES

- Bahcall, N., and Fan, X. 1998, ApJ, **504**, 1.  
 Brainerd, T.G., Wright, C.O., Goldberg, D.M., & Villumsen, J.V. 1999, ApJ, **524**, 9.  
 Cen, R. 1997, ApJ, **485**, 39.  
 Czoske, O., Soucail, G., & Kneib, J. 1999, in *Gravitational Lensing: Recent Progress and Future Goals*, eds. T.G. Brainerd and C.S. Kochanek (San Francisco: ASP), in press.  
 Evrard, A.E., Metzler, C.A., & Navarro, J.F. 1996, ApJ, **437**, 564.  
 Fahlman, G., Kaiser, N., Squires, G., & Woods, D. 1994, ApJ, **437**, 56.  
 Kaiser, N. 1995, ApJ, **439**, L1.  
 Kaiser, N., Wilson, G., Luppino, G., Kofman, L., Gioia, I., Metzger, M., & Dahle, H. 1999, ApJ, submitted. [astro-ph/9809268]  
 Kull, A., & Boehringer, H. 1999, A&A, **341**, 23.  
 Mellier, Y. 1999, *ARA&A*, **37**, 127. [astro-ph/9901116]  
 Metzler C., White M., Loken C., Norman M. 1999, ApJ, **520**, L9.  
 Miralda-Escude, J. 1991, ApJ, **380**, 1.  
 Norman, M.L., & Bryan, G.L., 1999, in *Numerical Astrophysics '98*, eds. S. Miyama, K. Tomisaka & T. Hanawa (Dordrecht: Kluwer), 19.  
 Norman, M.L., Daues, G., Nelson, E., Loken, C., Burns, J., Bryan, G., & Klypin, A. 2000, *Large-Scale Structure in the X-Ray Universe*, eds. M. Plionis & I. Georgantopoulos (Paris: Atlantisciences), 395.  
 Reblinsky, K., & Bartelmann, M. 1999, A&A, **345**, 1.  
 Scharf, C., Donahue, M., Voit, G.M., Rosati, P., & Postman, M. 1999, ApJ, **528**, L73.  
 Squires, G., Kaiser, N., Babul, A., Fahlman, G., Woods, D., Neumann, D.M., Boehringer, H. 1996, ApJ, **461**, 572.

- Wambsganss, J., Cen, R., & Ostriker, J.P. 1998, ApJ, **494**, 29.  
 van Haarlem, M.P., Frenk, C.S., & White, S.D.M. 1997, MNRAS, **287**, 817.